Waveguide Truncation Using UPML in the Finite-Element Time-Domain Method

Erik Abenius[1], Fredrik Edelvik[2] and Christer Johansson[3]

[1]Department of Information Technology, Uppsala University,
Box 337, SE-75105 Uppsala, Sweden
email: erik.abenius@it.uu.se

[2]Fraunhofer-Chalmers Research Centre for Industrial Mathematics,
Chalmers Science Park, SE-412 88 Göteborg, Sweden
email: fredrik.edelvik@fcc.chalmers.se

[3]Department of Numerical Analysis and Computer Science
Royal Institute of Technology, SE-100 44 Stockholm, Sweden
email: jnc@nada.kth.se

Abstract— An important part of numerical waveguide modeling is the termination of the waveguide using artificial boundaries. In this paper we develop a perfectly matched layer (PML) for waveguides in the finite-element time-domain method (FETD). The PML is discretized by prism elements aligned with the direction of propagation of the waveguide. Assuming that the waveguide is discretized by tetrahedra such a grid is easily generated from a cross-sectional surface in the waveguide. The proposed method has the advantage of being general with regard to the geometry and material of the waveguide. Previous works on PML for FETD have reported problems with late-time instability. While still present in the current approach, our results indicate that the instability is less severe for the prism element PML compared to a tetrahedral PML. Moreover, it may be controlled by increasing the number of grid points in the absorbing layer. It should be noted that the instability appears long after the energy has been attenuated and therefore pose no problems in practical computations. The performance of the suggested scheme is demonstrated for several waveguide problems, including an inhomogeneous case.

1 Introduction

The perfectly matched layer (PML) technique was introduced by Berenger in [1] for the finite-difference time-domain method, FDTD [2]. Berenger used a decomposition of the fields in Maxwell's equations to derive a lossy medium which allows reflectionless transmission of an incident plane wave from an arbitrary angle of incidence. By damping the wave in the direction normal to the interface between the PML and the exterior domain, the PML provides a means of truncating the computational domain. Later, it was shown in [3] that the non-physical field-splitting could be avoided and the PML be derived from Maxwell's equations in anisotropic media. This formulation, which is called the un-split or uniaxial PML (UPML), does not suffer from the weak well-posedness of the original PML which was shown in [4].

Furthermore, it is straightforward to generalize to anisotropic and dispersive media. Most of the research regarding PMLs is connected to FDTD, but PML has also been used in the frequency-domain finite-element method [5], [6] and more recently in the finite-element time-domain method (FETD) [7], [8]. In [9] a modification of the frequency-dependent attenuation function in [3] was introduced in the context of proving causality. Although it turned out that the modification was not needed for causality the modification had other useful properties. The resulting PML has later been labeled the complex frequency shifted PML (CFS-PML). In [10] numerical results were presented showing a late-time linear growth in the standard PML. The CFS-PML has been shown to remedy this problem [11] and further the attenuation of evanescent waves is improved [12]. In [13] they show convergence of the solution in a domain truncated by UPML to the solution of the unbounded problem for a second order finite-difference scheme in two dimensions.

In this paper we consider the termination of waveguides in FETD using a CFS-UPML for prism elements. The waveguide may be inhomogeneous in the transverse direction with one or more inner conductors. In order to minimize the reflections at the PML interface it is necessary to extend the material properties as well as conducting boundaries into the PML, such that the cross-sectional geometry is unchanged. Given a tetrahedral grid for the waveguide, a straightforward way of creating such a grid for the PML is offered by prism elements. The prisms are generated by an orthogonal translation of the triangulated surface in the waveguide cross-section (port), as illustrated in Figure 1. An advantage of this approach is that the discrete PML can be created automatically and need not be meshed by the unstructured grid generator.

In case of long integration times and few grid points in the absorbing layer the scheme exhibits numerical instability. This instability appears long after the energy of the system has been attenuated and the fields are close to zero. This property was also observed in [8] where a higher-order tetrahedral UPML was used. In our case the instability has only been observed for badly resolved cases and numerical results indicate that it may be controlled by increasing the resolution and the number of grid points in the PML. The latter property is not true for a tetrahedral discretization of the PML where the instability becomes more severe as the number of grid points in the PML increases. Another difference between our implementation and those in [7] and [8] is that we use a complex frequency shift formulation to improve attenuation of evanescent waves in the waveguide.

In the following section we will describe the implementation of an anisotropic PML absorber in the FETD method. Several numerical results are presented to illustrate the ability of the suggested scheme to truncate waveguides. Different waveguide geometries are considered including rectangular and coaxial as well as an inhomogeneous, shielded microstrip. Typically the transmission parameters for the basic mode of the waveguide are computed.

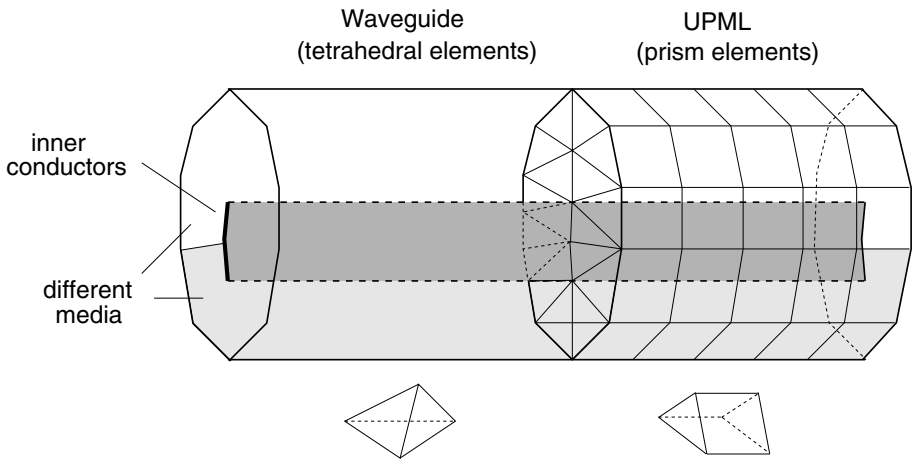

Figure 1: Waveguide truncation using UPML and prism elements.

2 Perfectly matched layer for prism elements in FETD

The Maxwell equations in the frequency domain are

$$\nabla \times \vec{E} = -j\omega \vec{B}, \tag{1}$$

$$\nabla \times \vec{H} = j\omega \vec{D} + \vec{J}, \tag{2}$$

where ω is the angular frequency and all vectors are functions of space, $\vec{r} \in \Omega$, and frequency, ω. The fields are related to the fluxes by constitutive relations. In dispersive (frequency-dependent) and anisotropic media they are

$$\vec{D} = \vec{\vec{\varepsilon}}(\omega) \cdot \vec{E}, \tag{3}$$

$$\vec{B} = \vec{\vec{\mu}}(\omega) \cdot \vec{H}, \tag{4}$$

where $\vec{\vec{\mu}}(\omega)$ where $\vec{\vec{\varepsilon}}(\omega)$ are tensors. Inserting the consitutive relations into the Maxwell equations and then multiplying (2) by $j\omega$ and using (1) to eliminate the magnetic field results in the vector wave equation for the electric field

$$-\vec{\vec{\varepsilon}}(\omega) \cdot \omega^2 \vec{E} + \nabla \times \left(\vec{\vec{\mu}}^{-1}(\omega) \cdot (\nabla \times \vec{E}) \right) = -j\omega \vec{J}. \tag{5}$$

The tensors are defined by

$$\vec{\vec{\mu}}(\omega) = \mu_0 \mu_r \vec{\vec{\Lambda}}(\omega),$$
$$\vec{\vec{\varepsilon}}(\omega) = \varepsilon_0 \varepsilon_r \vec{\vec{\Lambda}}(\omega),$$

where ε_0 and μ_0 are the permittivity and permeability of vaccum, ε_r and μ_r the relative values of the medium and $\vec{\vec{\Lambda}}(\omega)$ is a uniaxial tensor. The general form of the anisotropy for a three-dimensional unsplit PML in Cartesian coordinates is given by

$$\vec{\vec{\Lambda}}(\omega) = \frac{s_y s_z}{s_x} \hat{x}\hat{x} + \frac{s_x s_z}{s_y} \hat{y}\hat{y} + \frac{s_x s_y}{s_z} \hat{z}\hat{z},$$

where s_x, s_y and s_z are frequency dependent functions defined to attenuate the field in the x, y and z-directions, respectively. The tensor $\hat{x}\hat{x}$ denotes the outer product of the unit vector in the x-direction and correspondingly for $\hat{y}\hat{y}$ and $\hat{z}\hat{z}$. In the case of waveguide truncation it is sufficient to consider attenuation in the normal direction of the waveguide. For simplicity we will assume that the waveguide is oriented in the x-direction in the following derivations. In this case $s_y = 1$ and $s_z = 1$ resulting in

$$\vec{\vec{\Lambda}}(\omega) = s_x^{-1}\hat{x}\hat{x} + s_x\hat{y}\hat{y} + s_x\hat{z}\hat{z}. \tag{6}$$

Note that in the actual implementation the direction of the waveguide may be arbitrarily chosen. The attenuation function s_x is defined as

$$s_x(\omega) = \kappa + \frac{\sigma}{\alpha + j\omega\varepsilon_0}, \tag{7}$$

where σ is the conductivity and α and κ are real parameters. The original form of PML [1] corresponds to $\kappa = 1$ and $\alpha = 0$. However, the above complex frequency shifted form has been shown to have superior properties, particularly for the absorption of evanescent waves [12], [11], and is therefore used here.

Transformation to the time domain of (5) using the convention $j\omega \rightarrow \partial/\partial t$ leads to the equation

$$\vec{\vec{\varepsilon}}(t) \star \frac{\partial^2 \vec{E}}{\partial t^2} + \nabla \times \left(\vec{\vec{\mu}}^{-1}(t) \star (\nabla \times \vec{E}) \right) = \frac{\partial \vec{J}}{\partial t}, \tag{8}$$

where the convolution is defined as

$$[\vec{\vec{\Lambda}} \star \vec{E}](t) = \int_0^t \vec{\vec{\Lambda}}(\tau) \cdot \vec{E}(t-\tau) d\tau \,.$$

The elements of $\vec{\vec{\Lambda}}(t)$ are given by the Fourier transforms

$$s_x(\omega) \leftrightarrow s_x(t) = \kappa\delta(t) + \chi(t), \qquad \chi(t) = \bar{\sigma} e^{-\bar{\alpha}t} \bar{u}(t), \tag{9}$$

$$s_x^{-1}(\omega) \leftrightarrow s_x^{-1}(t) = \kappa^{-1}\delta(t) + \zeta(t), \qquad \zeta(t) = \frac{\bar{\sigma}}{\kappa^2} e^{-\left(\frac{\bar{\sigma}}{\kappa} + \bar{\alpha}\right)t} \bar{u}(t), \tag{10}$$

where $\bar{\sigma} = \sigma/\varepsilon_0$, $\bar{\alpha} = \alpha/\varepsilon_0$, $\delta(t)$ is the Dirac delta function and $\bar{u}(t)$ is the Heaviside step function. The weak formulation in the space dimension is obtained by introducing a suitable space W and then find $\vec{E} \in W$ such that for all $\vec{w} \in W$

$$\int_\Omega \left(\vec{w} \cdot \left(\vec{\vec{\varepsilon}}(t) \star \frac{\partial^2 \vec{E}}{\partial t^2} \right) + \nabla \times \vec{w} \cdot \left(\vec{\vec{\mu}}^{-1}(t) \star (\nabla \times \vec{E}) \right) \right) d\Omega = -\int_\Omega \vec{w} \cdot \frac{\partial}{\partial t} \vec{J} d\Omega, \tag{11}$$

where we have assumed a perfectly conducting outer boundary, $\hat{n} \times \vec{E} = \vec{0}$. We use linear edge elements [14] for the finite approximation of W, where tetrahedral elements are used inside the computational domain and prism elements in the PML.

Let the electric field be expanded according to

$$\vec{E}(\vec{r},t) = \sum_{j=1}^{M} E_j(t)\vec{N}_j(\vec{r}), \tag{12}$$

where M denotes the total number of basis functions and $\vec{N}_j$ denotes the j:th basis function. Using the Galerkin method, the test functions $\vec{w}$ are chosen as the basis functions $\vec{N}_i$. Assuming that the material properties are constant within each element the resulting system of ordinary differential equations becomes

$$\sum_{e=1}^{n_e} \left\{ K^e \frac{d^2\boldsymbol{E}}{dt^2} + S^e\boldsymbol{E} + K_1^e \frac{d^2\boldsymbol{\psi}}{dt^2} + S_x^e\boldsymbol{\psi} - K_x^e \frac{d^2\boldsymbol{\phi}}{dt^2} - S_1^e\boldsymbol{\phi} + \boldsymbol{f^e} \right\} = \mathbf{0} \tag{13}$$

where n_e is the total number of elements, $\boldsymbol{E}$ is a vector containing the unknowns $E_i(t), i = 1, \ldots, N$ and

$$\boldsymbol{\psi}(t) = \chi(t) \star \boldsymbol{E}(t), \tag{14}$$

$$\boldsymbol{\phi}(t) = \zeta(t) \star \boldsymbol{E}(t). \tag{15}$$

The vector $\boldsymbol{f}$ contains the source terms

$$(f^e)_i = \int_{\Omega^e} \vec{N}_i \cdot \frac{\partial}{\partial t}\vec{J}(\vec{r},t) d\Omega. \tag{16}$$

The elements of the matrices in (13) are

$$(K_x^e)_{ij} = \int_{\Omega^e} \varepsilon \left(\vec{N}_i \cdot \hat{x}\hat{x} \cdot \vec{N}_j \right) d\Omega\,, \tag{17}$$

$$(S_x^e)_{ij} = \int_{\Omega^e} \frac{1}{\mu} \left((\nabla \times \vec{N}_i) \cdot \hat{x}\hat{x} \cdot (\nabla \times \vec{N}_j) \right) d\Omega \tag{18}$$

$$(K_1^e)_{ij} = \int_{\Omega^e} \varepsilon \left(\vec{N}_i \cdot (\hat{y}\hat{y} + \hat{z}\hat{z}) \cdot \vec{N}_j \right) d\Omega\,, \tag{19}$$

$$(S_1^e)_{ij} = \int_{\Omega^e} \mu^{-1} \left((\nabla \times \vec{N}_i) \cdot (\hat{y}\hat{y} + \hat{z}\hat{z}) \cdot (\nabla \times \vec{N}_j) \right) d\Omega\,, \tag{20}$$

$$K^e = \kappa^{-1} K_x^e + \kappa K_1^e\,, \tag{21}$$

$$S^e = \kappa S_x^e + \kappa^{-1} S_1^e\,. \tag{22}$$

Assembling the local matrices in (13) results in the system

$$K\frac{d^2\boldsymbol{E}}{dt^2} + S\boldsymbol{E} + K_1\frac{d^2\boldsymbol{\psi}}{dt^2} + S_x\boldsymbol{\psi} - K_x\frac{d^2\boldsymbol{\phi}}{dt^2} - S_1\boldsymbol{\phi} + \boldsymbol{f} = \mathbf{0}. \tag{23}$$

Following the approach for frequency dispersive media used in [15] the system (23) is discretized by the second-order Newmark-Beta method [16] resulting in

$$\left(4K + \Delta t^2 S\right)\boldsymbol{E}^{n+1} = \left(8K - 2\Delta t^2 S\right)\boldsymbol{E}^n - \left(4K + \Delta t^2 S\right)\boldsymbol{E}^{n-1} - 4\Delta t^2 L^n \tag{24}$$

where Δt is the time step, $\boldsymbol{E}^n$ is the approximation of $\boldsymbol{E}(n\Delta t)$ and

$$L^n = K_1 \frac{d^2\boldsymbol{\psi}}{dt^2}^n + S_x \boldsymbol{\psi}^n - K_x \frac{d^2\boldsymbol{\phi}}{dt^2}^n - S_1 \boldsymbol{\phi}^n \,. \tag{25}$$

The convolution terms may be computed recursively using a centered piecewise constant approximation of the fields. We describe the procedure for the convolution

$$\boldsymbol{\upsilon}(t) = [\varphi \star \boldsymbol{E}](t)$$

where $\varphi(t) = ae^{-bt}$ and a and b are real constants. Assuming that $\boldsymbol{E}^n$ is constant in the centered time-interval $[(n-1/2)\Delta t, (n+1/2)\Delta t]$ and that $\boldsymbol{E}^0 = \boldsymbol{0}$ we have

$$\boldsymbol{\upsilon}^n = \int_0^{n\Delta t} \varphi(\tau)\boldsymbol{E}(n\Delta t - \tau)d\tau = \varphi^0 \boldsymbol{E}^n + \sum_{m=0}^{n-1} \boldsymbol{E}^{n-m-1}\varphi^{m+1/2} \tag{26}$$

where

$$\varphi^0 = \int_0^{\Delta t/2} \varphi(\tau)\boldsymbol{E}(n\Delta t - \tau)d\tau = \frac{a}{b}\left(1 - e^{-\frac{b\Delta t}{2}}\right) \tag{27}$$

$$\varphi^{m+1/2} = \int_{m+1/2}^{m+3/2} \varphi(\tau)\boldsymbol{E}(n\Delta t - \tau)d\tau = \frac{a}{b}\left(1 - e^{-b\Delta t}\right)e^{-b(m+1/2)\Delta t} \tag{28}$$

Noting that $\varphi^{m+1/2} = e^{-b\Delta t}\varphi^{m-1/2}$ the convolution $\boldsymbol{\upsilon}(t)$ can be written as a recursion

$$\boldsymbol{\upsilon}^n = \varphi^0 \boldsymbol{E}^n + \boldsymbol{\Upsilon}^n \tag{29}$$

$$\boldsymbol{\Upsilon}^n = \varphi^{1/2}\boldsymbol{E}^{n-1} + e^{-b\Delta t}\boldsymbol{\Upsilon}^{n-1} \tag{30}$$

The differentiated convolution terms in (23) are treated equivalently using that

$$\frac{d^2\boldsymbol{\upsilon}(t)}{dt^2} = \left[\varphi \star \frac{d^2\boldsymbol{E}}{dt^2}\right](t)$$

where we assume that $\boldsymbol{E}(0) = \boldsymbol{0}$ and $\frac{d\boldsymbol{E}}{dt}(0) = \boldsymbol{0}$. By substituting the constants a and b above by the corresponding values in (9) and (10) we obtain the expressions for the convolutions in (25). In order to give a more compact presentation we use the following notation for the second-order difference approximations

$$\ddot{\tilde{\boldsymbol{E}}}^n = \frac{\boldsymbol{E}^{n+1} - 2\boldsymbol{E}^n + \boldsymbol{E}^{n-1}}{\Delta t^2}\,,$$
$$\tilde{\boldsymbol{E}}^n = \frac{\boldsymbol{E}^{n+1} + 2\boldsymbol{E}^n + \boldsymbol{E}^{n-1}}{4}$$

. The time-stepping expressions for the Ψ terms in (25) becomes

$$\frac{d^2\boldsymbol{\psi}}{dt^2}^n = \chi^0 \ddot{\tilde{\boldsymbol{E}}}^n + \boldsymbol{\Psi}_1^n\,, \tag{31}$$

$$\boldsymbol{\Psi}_1^n = \chi^{1/2}\ddot{\tilde{\boldsymbol{E}}}^{n-1} + e^{-\bar{\alpha}\Delta t}\boldsymbol{\Psi}_1^{n-1}\,, \tag{32}$$

and

$$\boldsymbol{\psi}^n = \chi^0 \tilde{\boldsymbol{E}}^n + \boldsymbol{\Psi}_2^n \,, \tag{33}$$

$$\boldsymbol{\Psi}_2^n = \chi^{1/2} \tilde{\boldsymbol{E}}^{n-1} + e^{-\bar{\alpha}\Delta t} \boldsymbol{\Psi}_2^{n-1} \,, \tag{34}$$

where χ^0 and $\chi^{1/2}$ are given by (27) and (28)

$$\chi^0 = \frac{\bar{\sigma}}{\bar{\alpha}} \left(1 - e^{-\bar{\alpha}\frac{\Delta t}{2}}\right) \,, \tag{35}$$

$$\chi^{1/2} = \frac{\bar{\sigma}}{\bar{\alpha}} \left(1 - e^{-\bar{\alpha}\Delta t}\right) e^{-\bar{\alpha}\frac{\Delta t}{2}} \,. \tag{36}$$

The ϕ terms in (25) similarly become

$$\frac{d^2\boldsymbol{\phi}^n}{dt^2} = \zeta^0 \tilde{\ddot{\boldsymbol{E}}}^n + \boldsymbol{\Phi}_1^n \,, \tag{37}$$

$$\boldsymbol{\Phi}_1^n = \zeta^{1/2} \tilde{\ddot{\boldsymbol{E}}}^{n-1} + e^{-\left(\frac{\bar{\sigma}}{\kappa}+\bar{\alpha}\right)\Delta t} \boldsymbol{\Phi}_1^{n-1} \,, \tag{38}$$

and

$$\boldsymbol{\phi}^n = \zeta^0 \tilde{\boldsymbol{E}}^n + \boldsymbol{\Phi}_2^n \,, \tag{39}$$

$$\boldsymbol{\Phi}_2^n = \zeta^{1/2} \tilde{\boldsymbol{E}}^{n-1} + e^{-\left(\frac{\bar{\sigma}}{\kappa}+\bar{\alpha}\right)\Delta t} \boldsymbol{\Phi}_2^{n-1} \,, \tag{40}$$

where the constants are given by

$$\zeta^0 = \frac{\bar{\sigma}}{\kappa(\bar{\sigma} + \kappa\bar{\alpha})} \left(1 - e^{-\left(\frac{\bar{\sigma}}{\kappa}+\bar{\alpha}\right)\frac{\Delta t}{2}}\right) \,, \tag{41}$$

$$\zeta^{1/2} = \frac{\bar{\sigma}}{\kappa(\bar{\sigma} + \kappa\bar{\alpha})} \left(1 - e^{-\left(\frac{\bar{\sigma}}{\kappa}+\bar{\alpha}\right)\Delta t}\right) e^{-\left(\frac{\bar{\sigma}}{\kappa}+\bar{\alpha}\right)\frac{\Delta t}{2}} \,. \tag{42}$$

In the case where $\kappa = 1$ and $\bar{\alpha} = 0$ $\chi(t) = \bar{\sigma}\bar{u}(t)$ is constant (for $t > 0$) resulting in

$$\chi^0 = \frac{\bar{\sigma}\Delta t}{2} \,, \tag{43}$$

$$\chi^{1/2} = \bar{\sigma}\Delta t \,. \tag{44}$$

and equations (31)-(34) are reduced to

$$\frac{d^2\boldsymbol{\psi}^n}{dt^2} = \frac{\bar{\sigma}\Delta t}{2} \tilde{\ddot{\boldsymbol{E}}}^n + \boldsymbol{\Psi}_1^n \,, \tag{45}$$

$$\boldsymbol{\Psi}_1^n = \bar{\sigma}\Delta t \tilde{\ddot{\boldsymbol{E}}}^{n-1} + \boldsymbol{\Psi}_1^{n-1} \,, \tag{46}$$

$$\boldsymbol{\psi}^n = \frac{\bar{\sigma}\Delta t}{2} \tilde{\ddot{\boldsymbol{E}}}^n + \boldsymbol{\Psi}_2^n \,, \tag{47}$$

$$\boldsymbol{\Psi}_2^n = \bar{\sigma}\Delta t \tilde{\ddot{\boldsymbol{E}}}^{n-1} + \boldsymbol{\Psi}_2^{n-1} \,. \tag{48}$$

The corresponding equations for the Φ and $\frac{d^2\Phi}{dt^2}$ terms are obtained by setting $\kappa = 1$ and $\bar{\alpha} = 0$ in (37)–(40).

3 Numerical results

The proposed PML is evaluated by five different test cases. Case 1 is a parallel plate waveguide where the reflection from a plane wave impinging on a PML is studied. In this case we also determine the error in the Huygens' surface which is used to generate the field. This error affects the backscattered field computed in cases 2-4. In Case 2 the PML is used for truncation of a rectangular waveguide. Ports are used for excitation and registration of the basic TE10 mode and the scattering parameters are computed. In Case 3 we consider termination of a dielectric coaxial waveguide and Case 4 consists of a shielded microstrip waveguide where the basic mode is a quasi-TEM mode. In Case 5 we address late-time instability which is observed for badly resolved geometries and few grid points in the PML layer.

In all cases we use the complex frequency shifted form (7) where $\alpha = 0.05$ and $\kappa = 1.0$. The conductivity is gradually increased in the PML according to a quadratic polynomial,

$$\sigma(\rho) = \sigma_{max} \left(\frac{\rho}{d}\right)^2 , \qquad \sigma_{max} = -\frac{3\varepsilon_0 c_0 \log(R_0)}{2d} \tag{49}$$

where ρ is the orthogonal distance from the PML interface, d is the width of the PML and R_0 is the theoretical reflection coefficient. The PML is discretized by linear prism elements with constant height and the number of grid points in the ρ direction is denoted by n_l.

Case 1 - TEM mode in a parallel plate waveguide. The geometry consists of a rectangular waveguide oriented in the x-direction with PMC (perfect magnetic conductor) boundary conditions in the y-direction and PEC (perfect electric conductor) boundary conditions in the z-direction. This geometry supports a TEM mode with (E_z,H_y)-polarization. The geometry is illustrated in Figure 2.

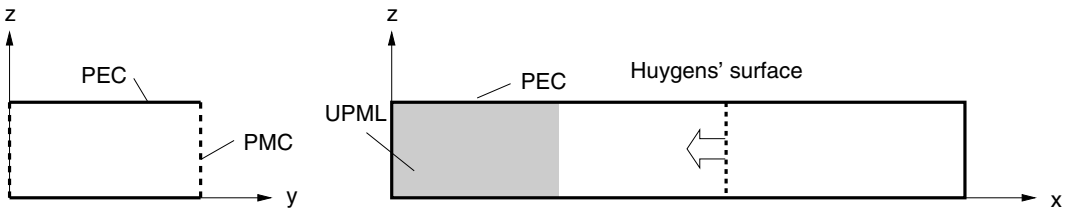

Figure 2: The geometry for the parallel plate waveguide problem.

The excitation has the form a modulated Gaussian pulse,

$$f(t) = \sin\left(2\pi f_0(t - t_0)\right) e^{-(\frac{t-t_0}{t_w})^2} \tag{50}$$

where f_0 is the center frequency, t_0 is the center time and t_w governs the width of the pulse. This function is well localized both in time and frequency, as illustrated in Figure 3. As a result, time-gating can be used to isolate reflections from different parts of the geometry while at the same time spectral information is available through the sinusoidal part.

The plane wave is generated by a Huygens' surface [17] and the field is probed in the total-field region. The length of the waveguide and the width of the pulse are chosen such that the reflection from the boundary and the incident field are well

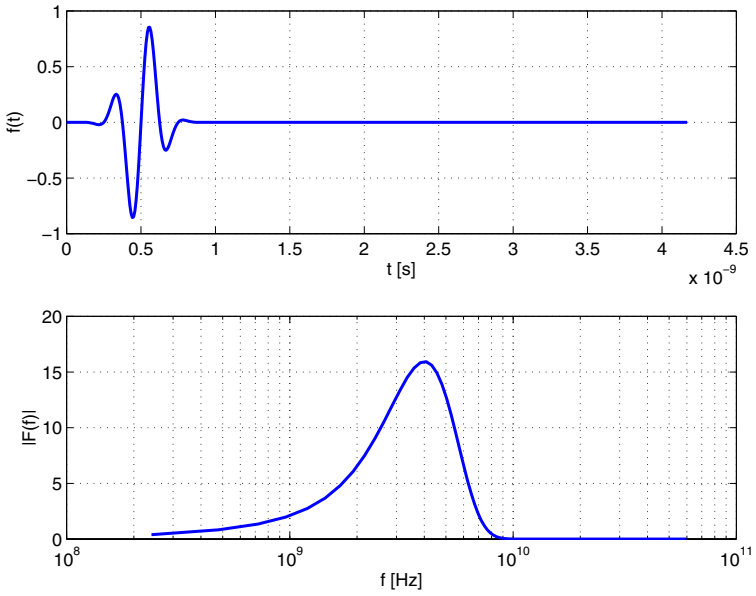

Figure 3: The modulated Gaussian pulse in the time-domain (above) and the frequency-domain (below). The parameters are $t_0 = 0.5 \cdot 10^{-9}$ s, $t_w = 0.15 \cdot 10^{-9}$ s and $f_0 = 4$GHz.

separated in time. The waveguide is discretized by a tetrahedral grid generated by splitting the cells of a uniform cubical grid. One end of the waveguide is terminated by PML and the other by a PEC. The absorbing layer is truncated by a PEC wall.

The transition from tetrahedral elements to prism elements at the start of the PML will cause numerical reflections. This error is independent of the absorbing properties of the PML and therefore constitute a lower bound on the performance of the PML. In order to measure the transition error the material properties of the PML are set to free space and the layer is extended sufficiently far to avoid interference from the field reflected from the PEC wall. In Figure 4 the computed reflection error is plotted as a function of the resolution in grid points per wavelength for three different grid sizes $h = 0.01, 0.005$ and 0.0025m. Theoretically, the error should decrease as h^2 corresponding to a decrease of 12dB when h is halved. This agrees very well with the observed errors in Figure 4 noting that the errors should be compared at the same wavelength (not the same resolution). The results verify that the reflection caused by the transition between the two element types can be controlled by increasing the resolution of the grid. However, the error may well be of the same magnitude as the reflection caused by the PML, particularly for badly resolved problems.

We now study the reflection errors for a waveguide truncated by PML. Figure 5 shows the results for three different PMLs on the finest grid where $h = 0.0025$m. For the case of $n_l = 8$ the reflection error is around -50dB over the entire frequency interval. Increasing the width of the PML clearly improves the results and the error is around -65dB for $n_l = 16$. For $n_l = 32$ the errors are close to the level of the element transition, shown in Figure 4. Further extending the PML will consequently not lead to any significant decrease in the reflection error. Note that the performance of the PML not only depends on the number of grid points but also the physical width of the absorbing layer. In Case 3 and 4 where different resolutions are compared, we therefore maintain the width of the PML when refining the grid.

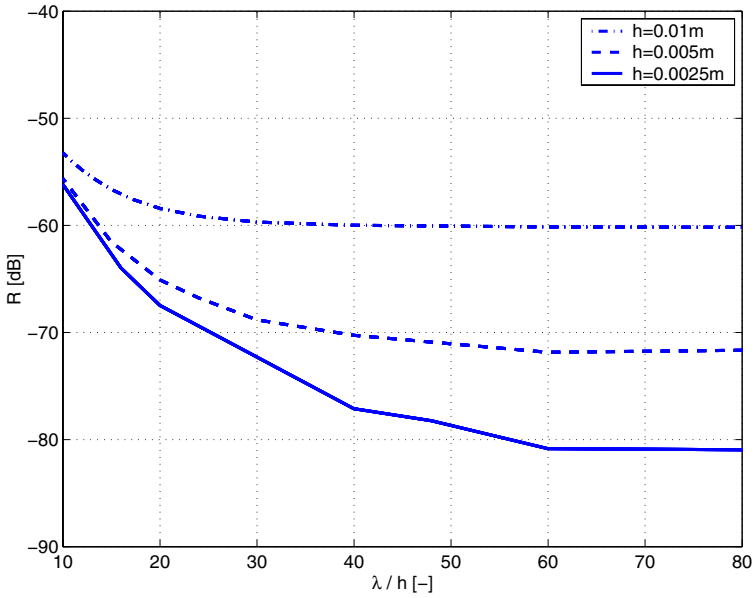

Figure 4: Parallel plate case: reflection error from the transition between prisms and tetrahedra.

The incident field is generated by a Huygens' surface which divides the waveguide into a scattered-field and a total-field region. Due to numerical errors a wave traveling backwards from the surface into the scattered field region will also be generated. In many cases this is not a problem since absorbing boundary conditions prevent the wave from entering the total-field region. However, in the waveguide results presented later, the field propagating backwards from an excitation port is registered and affects the computed scattering parameters. In Figure 6, we show the relative amplitude of the backward wave for different grid sizes and frequencies. The reflection from the PML is not taken into account in these results. The observed error is proportional to h. Note that this error does not affect the results shown in Figures 4 and 5 where we only measure the reflections caused by the transition and the PML.

Case 2 - TE mode in a rectangular waveguide. In this case the geometry consists of an empty rectangular waveguide with PEC walls. The cross-section of the waveguide has dimensions $2a$ by a as illustrated in Figure 7. The waveguide is fed by the dominant TE10 mode modulated by a broadband pulse in the frequency-domain. The pulse consist of a unitary rectangular pulse terminated at each end by half Gaussian pulses. Figure 8 shows the excitation in the time and frequency domains.

The waveguide is discretized by a tetrahedral grid and is truncated by PML in the two ports, as illustrated in Figure 7. The mode field excitation is generated in Port 1 and the S_{11} and S_{12} (transmitted energy from Port 1 to Port 2) parameters are computed. In this case an analytical mode field was used. Since no obstacles are present in the waveguide S_{11} should be zero and S_{12} should be one. The results for a waveguide with a=0.1m are shown in Figure 9. We have included results using a simple first-order absorbing boundary condition (ABC) for comparison. Two different grid sizes are used, corresponding to edge lengths of h=0.01m and h=0.005m. In the given frequency range the resolution is thus between 10 and 60 points per

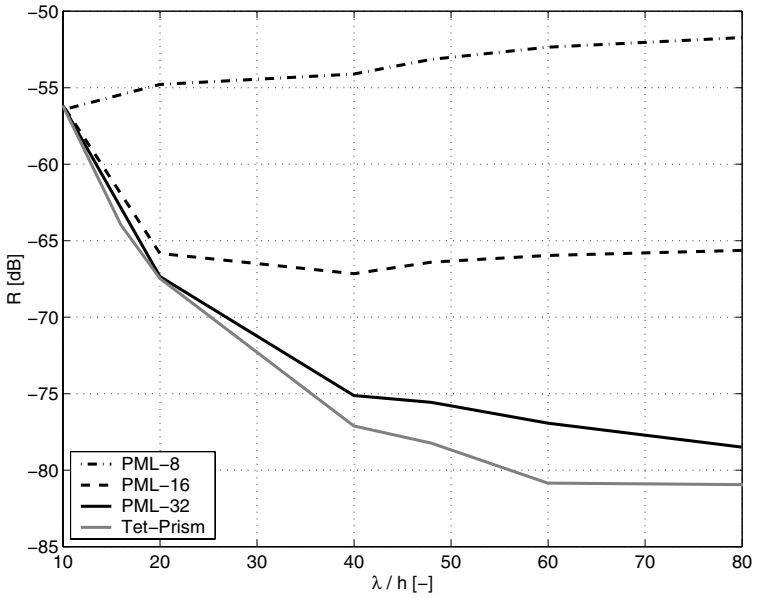

Figure 5: Reflection error for PML truncation of the parallel plate waveguide for h=0.0025. The gray curve is the reflection error for the interface between tetrahedra and prisms at the beginning of the PML (shown in Figure 4).

wavelength on the coarse grid and between 20 and 120 on the fine grid. The cutoff frequency for the TE10 mode is 0.75GHz which is clearly seen in the results as a peak in the S_{11} curves. Above the cutoff frequency S_{11} lies in the range of -50dB to -30dB on the coarse grid and about 10dB lower on the fine grid. Increasing the width of the PML does not lead to any significant improvement of the S_{11} results. This indicates that other error sources, such as the backward propagating wave in the excitation port (see Figure 6) affect the S_{11} parameter. The performance of the PML is therefore better estimated from the S_{12} parameter since it does not suffer from the error in the excitation port. The RMS errors in the scattering parameters for the frequency range from 1GHz to 3GHz are found in Table 1.

Table 1: RMS error in the scattering parameters for the rectangular waveguide in the frequency range 1-3GHz.

h [mm]	n_l	S_{11} [dB]	S_{12} [dB]
10	8	-36	-51
10	16	-37	-58
5	16	-43	-66
5	32	-43	-72
10	ABC	-23	-24
5	ABC	-23	-23

As expected the error in S_{12} is considerably smaller than in S_{11} and corresponds very well with the plane wave results in Figure 5.

Case 3 - TEM mode in a coaxial waveguide. One of the major advantages with the unstructured finite element approach compared to standard FDTD is the

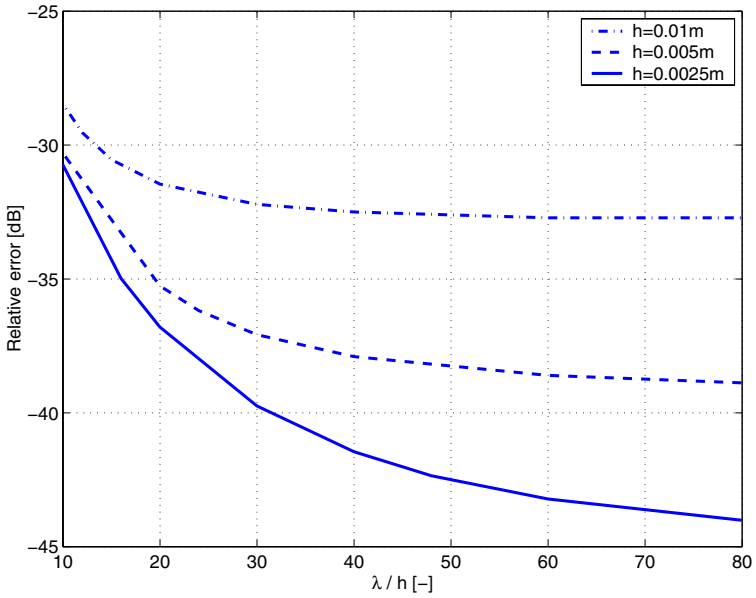

Figure 6: The relative amplitude of the backward wave from a Huygens' surface computed as the quotient between the maximum amplitudes of the backward and the forward propagating waves.

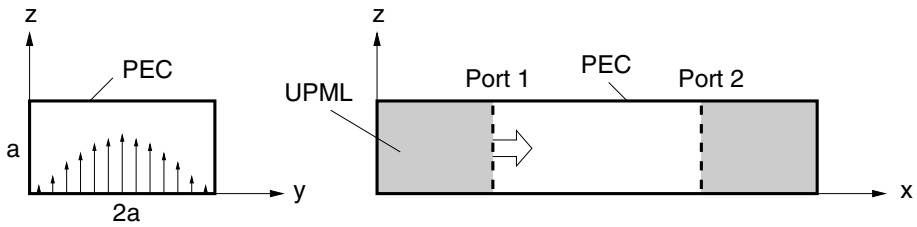

Figure 7: The geometry for the rectangular waveguide problem. The arrows in the left figure show the field distribution of the basic TE10 mode.

ability to accurately model curved boundaries. In the previous example FDTD, would most likely be more efficient since the geometry fits very well in a Cartesian mesh. In this case however, the geometry consists of a circular coaxial waveguide, as illustrated in Figure 10. The inner radius is 1mm and the outer radius is 2mm and the waveguide is filled with a dielectric media with relative permittivity, ε_r=2. The waveguide is fed by the TEM mode in Port 1 and we wish to compute S_{11} and S_{12} which should be zero and one, respectively. The mode field is computed using an analytical expression. Two different grids were used, corresponding to edge lengths of h=0.5mm and h=0.25mm. The waveguide is truncated by PMLs in the ports which are located at a distance of 10mm from each other. The computed results are shown in Figure 11. The resolution on the coarse grid ranges from about 10 points per wavelength at 60GHz to 60 at 10GHz and from 20 to 120 points per wavelength on the fine grid. As discussed in the previous case, S_{11} should not be interpreted as the reflection caused by the PML due to errors in the excitation. The RMS errors are given in Table 2.

Case 4 - Quasi-TEM mode in a shielded microstrip waveguide. In this case we consider an inhomogeneous waveguide. The cross-section consists of two different media and an infinitely thin interior conductor enclosed in an outer rectangular PEC

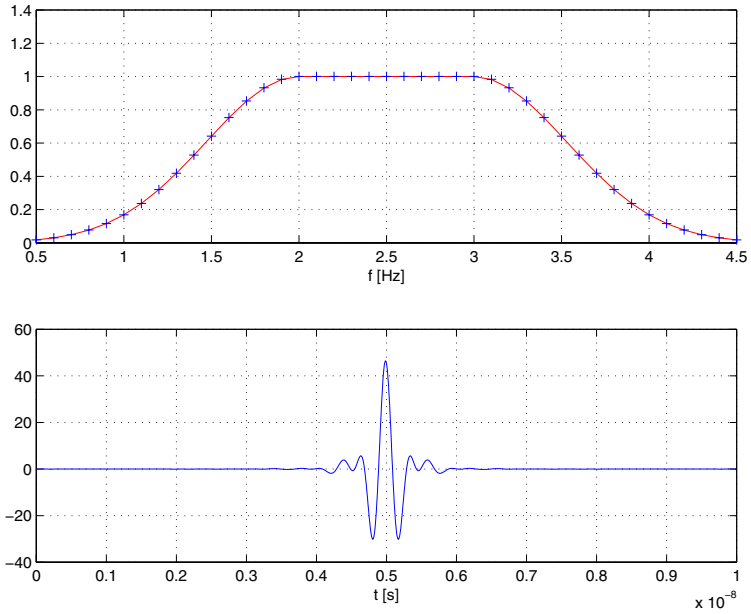

Figure 8: Amplitude scaling of the incident TE10 wave.

Table 2: RMS error in the scattering parameters for the coaxial waveguide in the frequency range 10-40GHz.

h [mm]	n_l	S_{11} [dB]	S_{12} [dB]
0.5	8	-34	-51
0.5	16	-34	-50
0.25	16	-40	-53
0.25	32	-40	-58

wall. The geometry is illustrated in Figure 12. The fundamental mode of this type of waveguide is a quasi-TEM mode. There is no closed form expression for the mode field, hence it has to be computed numerically. For this case we have used an edge-element, finite-element mode solver for the full vector Helmholtz equation in the cross-section of the waveguide, see [17],[18]. The mode solver uses the ARPACK library for the resulting generalized eigenvalue problem. Note that the mode solver uses the cross-sectional grid from the 3-D model. The S_{11} and S_{12} parameters were computed for the case of a=0.1m and an edge length of h=0.005m in the tetrahedral grid. The results are shown in Figure 13. The free space resolution ranges from about 17 points per wavelength at 3.5GHz to 40 points per wavelength at 1.5GHz. However, the major part of the energy is contained in the dielectric region where the resolution is only half of that in free space. The RMS errors of the scattering parameters are shown in Table 3. The discrepancy between the errors in S_{11} and S_{12} again indicate that the main contribution to S_{11} comes from errors in the excitation. The error in S_{12} does not decrease by any significant amount when the width of the PML is increased.

Case 5 - Late-time instability. The proposed scheme suffers from instability occurring for long integration times. However, the instability appears long after

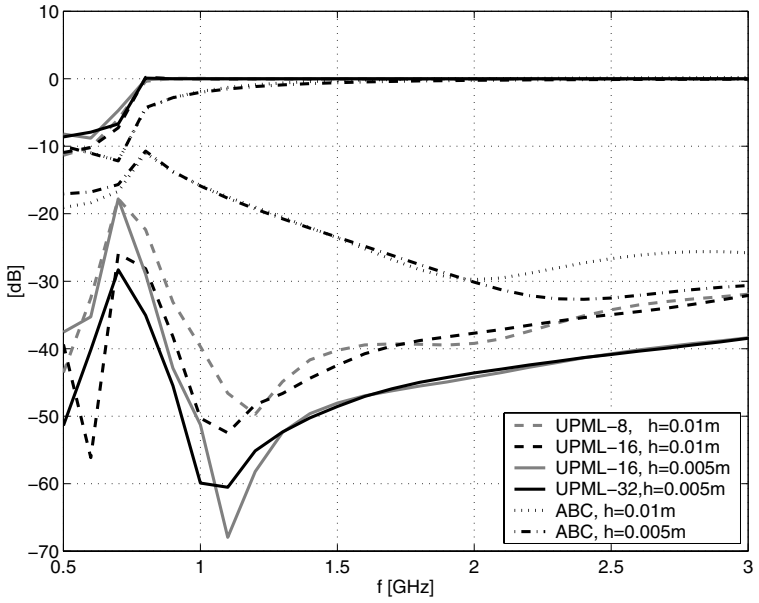

Figure 9: S_{11} and S_{12} for the TE10 mode in the rectangular waveguide.

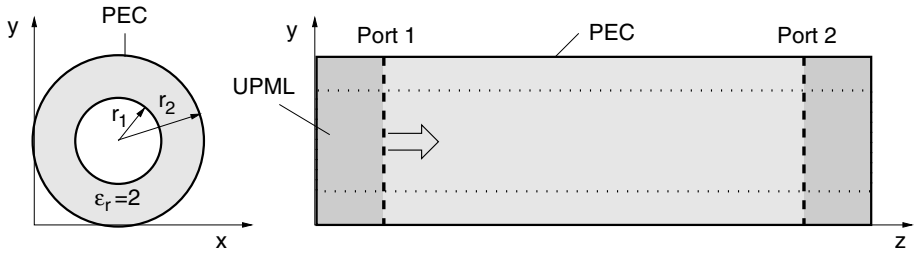

Figure 10: The geometry for the coaxial waveguide problem.

the energy has dissipated and therefore does not cause any problems in practical computations. Furthermore, the instability can be delayed by extending the PML. For the purpose of studying the late-time instability we use a test problem consisting of an empty rectangular waveguide terminated by PML in one end and by PEC in the opposite end. The waveguide is fed by a TE10 wave in an excitation port located at the interface to the PML layer and the field is probed inside the waveguide. The tetrahedral grid is generated by splitting the cells of a uniform cubical lattice with 8×4 cells in the cross section and 10 cells between the beginning of the PML and the opposite PEC wall. The probed field for different PML sizes are shown in Figure 14. In the case of $n_l = 4$, i.e. four grid points in the width direction of the PML, the instability becomes visible after about 35000 iterations, for $n_l = 8$ it appears after 150000 iterations and for $n_l = 12$ it takes until 450000 iterations. Note that

Table 3: RMS error in the scattering parameters for the shielded microstrip waveguide in the frequency range 1.5-3.5GHz.

h [mm]	n_l	S_{11} [dB]	S_{12} [dB]
10	8	-33	-57
10	16	-33	-61

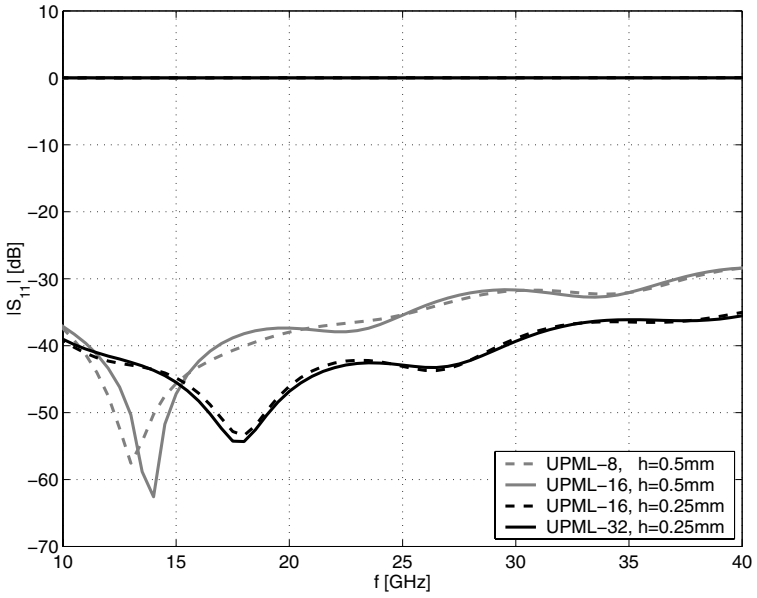

Figure 11: S_{11} and S_{12} for the TEM mode in the coaxial waveguide.

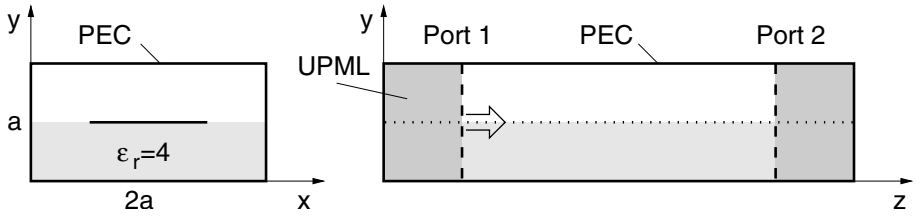

Figure 12: The geometry of the shielded microstrip waveguide.

the fields are very small when the instability occurs. Additional experiments have shown that the instability may be further delayed by lowering R_0 (i.e. increasing the conductivity scaling). As a comparison, we did the same experiment using a tetrahedral grid for the PML. The grid was generated from a cubical lattice by splitting each cube into five tetrahedra. The results are shown in Figure 15. In this case the instability appears much earlier. Furthermore, the growth rate of the instability increases as the number of grid points in the PML is increased. For $n_l = 4$ the instability becomes visible after about 7000 iterations, for $n_l = 8$ after 4500 iterations and for $n_l = 12$ after about 4000 iterations.

4 Conclusion

We have presented an implementation of the complex-frequency shifted UPML on prism elements for truncating waveguides in the time-domain finite-element method. The proposed method has been successfully applied to a number of waveguide problems, including inhomogeneous waveguides with interior conductors. Error levels as low as -70 dB in the scattering parameters have been shown for realistic waveguide problems. The problem of late-time instability discussed in previous implementations of PML in FETD is not completely remedied. However, our results indicate that the prism element PML is more robust than PMLs based on tetrahedra. Further, the use of prism elements allows automatic generation of the PML grid, even

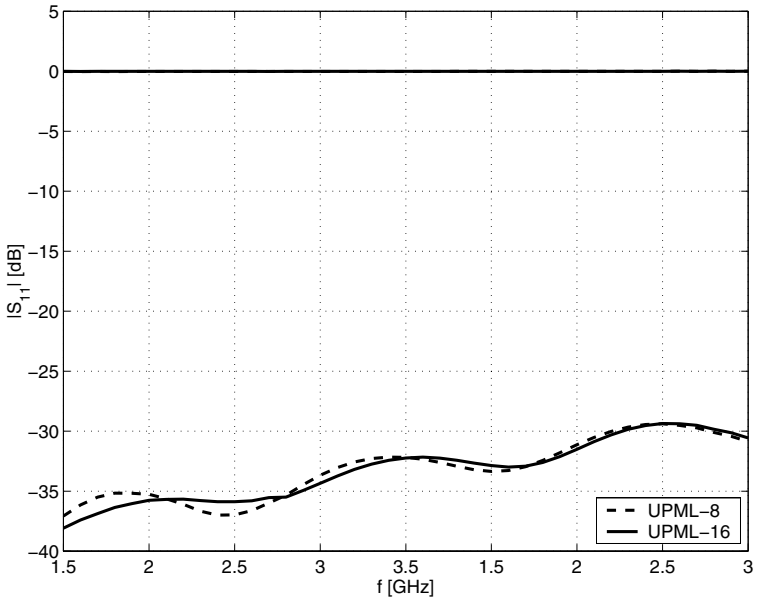

Figure 13: S_{11} and S_{12} for the quasi-TEM mode in the shielded microstrip waveguide.

in case of complex waveguide cross-sections.

5 Acknowledgments

Financial support has been provided by the Parallel and Scientific Computing Institute (PSCI) and the Swedish Foundation for Strategic Research (SSF).

References

[1] J-P. Berenger. A perfectly matched layer for the absorption of electromagnetic waves. *J. Comput. Phys.*, 114(1):185–200, 1994.

[2] A. Taflove and S. C. Hagness. *Computational Electrodynamics: The Finite-Difference Time-Domain Method, Third Edition.* Artech House, Boston, MA, 2005.

[3] Z. S. Sacks, D. M. Kingsland, R. Lee, and J. F. Lee. A perfectly matched anisotropic absorber for use as an absorbing boundary condition. *IEEE Trans. Antennas Propagat.*, 43(12):1460–1463, 1995.

[4] S. Abarbanel and D. Gottlieb. A mathematical analysis of the PML method. *J. Comput. Phys.*, 134:357–363, 1997.

[5] J. Y. Wu, D. M. Kingsland, J. F. Lee, and R. Lee. A comparison of anisotropic PML to berenger's PML and its application to the finite-element method for EM scattering. *IEEE Trans. Antennas Propagat.*, 45(1):40–50, January 1997.

[6] M. Kuzuoglu and R. Mittra. Investigation of nonplanar perfectly matched absorbers for finite-element mesh truncation. *IEEE Trans. Antennas Propagat.*, 45(3):474–486, March 1997.

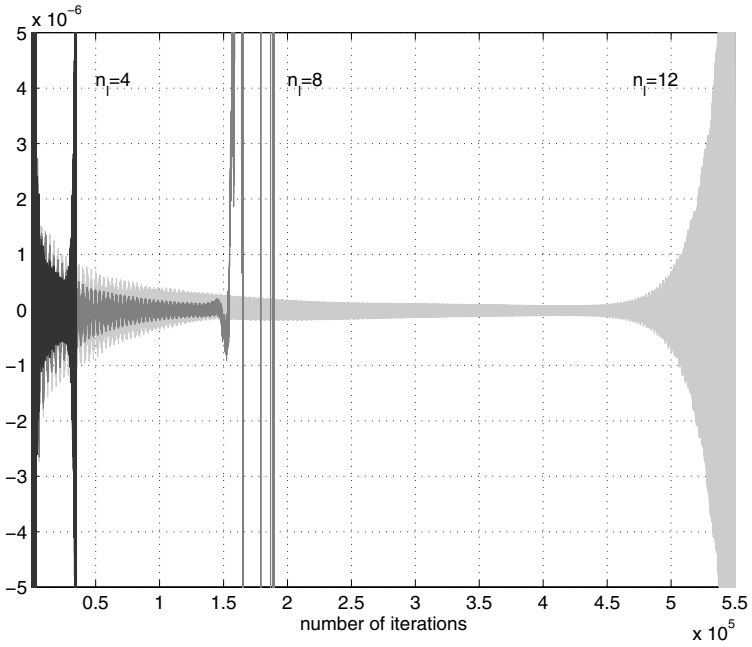

Figure 14: Late-time instability for the prism PML. The probed field for three different PML sizes: $n_l = 4$ (dark grey),$n_l = 8$ (grey) and $n_l = 12$ (light grey). $R_0 = 0.001$ in all cases.

[7] D. Jiao, J-M. Jin, E. Michielssen, and D. Riley. Time-domain finite-element simulation of three-dimensional scattering and radiation problems using perfectly matched layers. *IEEE Trans. Antennas Propagat.*, 51(2):296–305, February 2003.

[8] T. Rylander and J-M. Jin. Perfectly matched layer in three dimensions for the time-domain finite element method applied to radiation problems. *IEEE Trans. Antennas Propagat.*, 53(4):1489–1499, April 2005.

[9] M. Kuzuoglu and R. Mittra. Frequency dependence of the constitutive parameters of causal perfectly matched anisotropic absorbers. *IEEE Microwave Guided Wave Lett.*, 6(12):447–449, December 1996.

[10] S. Abarbanel, D. Gottlieb, and J. S. Hesthaven. Long time behaviour of the perfectly matched layer equations in computational electromagnetics. *Journal of Scientific Computing*, 17(1-4):405–422, 2002.

[11] E. Becache, P. Petropoulos, and S. Gedney. On the long-time behavior of unsplit perfectly matched layers. *IEEE Trans. on Antennas and Propagat.*, 52:1335–1342, May 2004.

[12] J-P. Berenger. Application of the CFS PML to the absorption of evanescent waves in waveguides. *IEEE Microw. and Wireless Comp. Lett.*, 12(6):218–220, June 2002.

[13] B. Sjögreen and N. A. Petersson. Perfectly matched layers for Maxwell's equations in second order formulation. *J. Comput. Phys.*, 209:19–46, 2005.

[14] J. Jin. *The Finite Element Method in Electromagnetics*. Wiley, New York, 2nd edition, 2002.

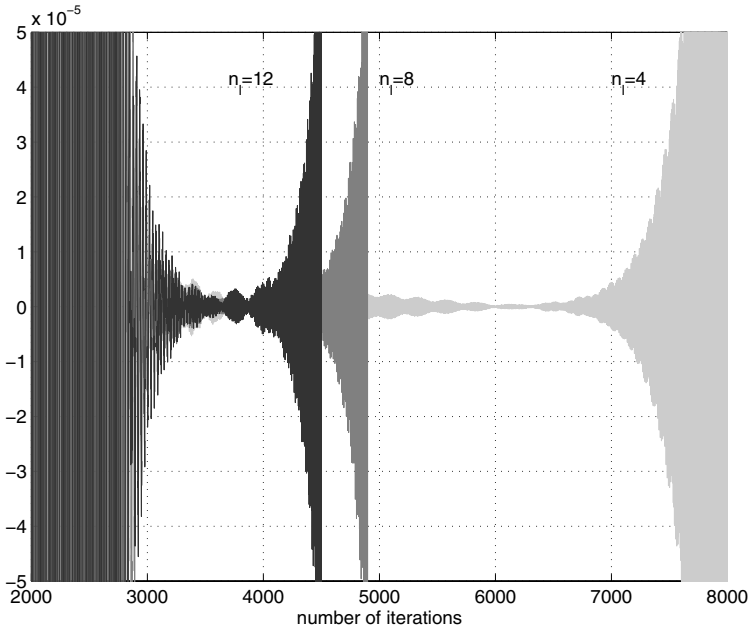

Figure 15: Late-time instability for the tetrahedral PML. The probed field for three different PML sizes: $n_l = 4$ (light grey),$n_l = 8$ (grey) and $n_l = 12$ (dark grey). $R_0 = 0.001$ in all cases.

[15] F. Edelvik and B. Strand. Frequency dispersive materials for 3D hybrid solvers in time domain. *IEEE Trans. Antennas Propagat.*, 51(6):1199–1205, June 2003.

[16] T. J. R. Hughes. *The Finite Element Method: Linear Static and Dynamic Finite Element Analysis*. Prentice-Hall, Englewood Cliffs, NJ, 1987.

[17] E. Abenius and C. Johansson. Modeling of inhomogeneous waveguides using hybrid methods. *submitted to Int. Journal of Numerical Modelling: Electronic Networks, Devices and Fields*, 2005.

[18] C. Johansson. *Numerical Methods for Ports in Closed Waveguides*. Lic. thesis, Department of Numerical Analysis and Computer Science, Royal Institute of Technology, Stockholm, Sweden, October 2003.